Energy Storage Materials 46 (2022) 352–365

Contents lists available at ScienceDirect

Energy Storage Materials

journal homepage: www.elsevier.com/locate/ensm

An efficient gel polymer electrolyte for dendrite-free and long cycle life lithium metal batteries

Vahid Jabbari, Vitaliy Yurkiv, Md Golam Rasul, Mahmoud Tamadoni Saray, Ramin Rojaee, Farzad Mashayek, Reza Shahbazian-Yassar*

Department of Mechanical and Industrial Engineering, University of Illinois at Chicago, Chicago, IL 60607, USA

ARTICLE INFO

Keywords:
Gel polymer electrolyte
Dendrite-free Li electrodeposition
LiF-rich interface
Lithium metal battery
Long cycle life

ABSTRACT

Lithium metal batteries (LMBs) are plagued with non-uniform and dendritic electrodeposition of Li when used with liquid electrolytes, resulting in poor cycle life and Coulombic efficiency, and safety hazards. Herein, we report a novel gel polymer electrolyte (GPE) for LMBs enabling uniform and nondendritic Li electrodeposition, long cycle life, and high Columbic efficiency. The GPE is made by immobilization of liquid electrolytes within a crosslinked polymer matrix. At ambient temperature, the GPE shows a Li ion conductivity of 1.5 mS cm^{-1}. Topology and morphology of the electrochemically deposited Li in the GPE were studied by *operando* optical microscopy and scanning electron microscopy (SEM). Cryogenic transmission electron microscopy (cryo-TEM) and X-ray photon spectroscopy (XPS) characterizations indicate that the solid electrolyte interphase (SEI) layer at the Li/GPE interface is a thin and LiF-rich while the SEI layer is thick and LiF-poor at the Li/liquid electrolyte interface. Density functional theory (DFT) calculations show that LiF crystals facilitate and regulate Li ions transport. Lithium|lithium iron phosphate (Li|LFP) cells with our GPE deliver an initial specific capacity of ~130 mAh g^{-1} and ~70% capacity retention after 1000 cycles at 2C charge/discharge rate. This study offers a promising approach for engineering a stable and conductive Li/polymer electrolyte interface for dendrite-free LMBs.

1. Introduction

Li metal is an ultimate anode for future high-energy-density rechargeable batteries, when in combination with high-capacity cathodes [1]. This is because of unique properties of Li metal including lightweight (0.59 g cm^{-3}), high specific capacity (3860 mAh g^{-1}), and low reduction potential (−3.040 V vs. SHE) [2]. However, commercial applications of lithium metal batteries (LMBs) are impeded by critical issues of poor cycle life and Columbic efficiency (CE), and safety hazards that are correlated with dendritic growth of Li during plating/stripping processes [3–8]. In general, the dendritic Li induces fragility to the Li metal electrodeposits which can result in pulverization of the Li deposit, producing dead or inactive Li [9,10]. This phenomenon can accelerate the electrolyte degradation and induces capacity loss, poor reversibility and low CE, and also can cause safety hazards such as cell shorting and thermal runaway [11]. Therefore, the intrinsic chemical reactivity of Li metal, that reacts with almost all organic liquid electrolytes, make liquid electrolytes unsuitable in LMBs [11,12]. Besides, flammability, toxicity, and solvent leakage further hinder practical commercial applications of LMBs when used with liquid electrolytes [13,14].

Owing to high Li ion conductivity (10^{-3}-10^{-2} S cm^{-1}) at ambient temperature and good electrode-electrolyte interfacial contact, gel polymer electrolytes (GPEs) are promising alternative to liquid electrolytes [8,15,16]. Indeed, a GPE made of a polymer matrix swollen by a liquid electrolyte can combine the advantages of the liquid electrolyte and solid component in a single system [13,17–20]. Stemming from high electrochemical stability, flexibility, electrically insulating nature, high Li ion solvating strength, compatibility with Li metal, and ability to effectively coordinate and regulate Li ions transport, polyethylene oxide (PEO) is shown to be the most promising candidate for polymer electrolytes [13,17–19]. Most of previous works on PEO-based GPEs crosslink a regular PEO in the presence of a Li salt and/or solvent using large amount of radical initiators [13,19–21]. Those approaches suffer from several drawbacks: (i) Crosslinking occurs in the PEO backbone, decreasing the PEO chains mobility and hence, ionic conductivity of GPE [17]; (ii) There is a limitation and lack of control on the degree of crosslinking, leading to nonuniform chemistry or structure of the resulting GPE [21]; (iii) Initial composition of GPE can be altered by evaporation of solvents/liquids stimulated by light or heat during crosslinking process [13,19,20]; (iv) Using a radical initiator (up to 10 wt.%) can alter the original structure or chemistry of solid electrolyte interphase (SEI) with detrimental effect on electrochemical performance [13,21]. Short chain length PEO, also called polyethylene glycol (PEG), with self-crosslinkable ability, for example, polyethylene glycol diacrylate (PEGDA), are also used to synthesize GPEs. Nevertheless,

* Corresponding author.
E-mail address: rsyassar@uic.edu (R. Shahbazian-Yassar).

https://doi.org/10.1016/j.ensm.2022.01.031
Received 18 September 2021; Received in revised form 30 December 2021; Accepted 16 January 2022
Available online 18 January 2022

GPEs made of a crosslinked network with short chain length polymers or oligomers demonstrate poor mechanical strength [19], and these polymer matrixes usually are used in conjunction with a support/separator, for example, cellulose acetate [19]. GPEs made using such oligomers typically also present a poor ionic conductivity or electrochemical performance [13,18,19]. It is well-known that ionic conduction in PEO is mainly governed by hooping of Li ions through free and dynamic polymer chains [21]. Thus, short polymeric chains with limited mobility within a crosslinked matrix result in a poor ionic conduction and electrochemical performance [13,14,20]. Additionally, GPEs made using a short chain length PEG are thermally unstable, as a low degradation onset temperature is identified by thermogravimetric analysis (TGA) [13,14,19]. For example, Liu et al. reported a GPE made using oligomeric PEGDA (molar mass of 400) which decompose below 250 °C [13].

Herein, we report a novel GPE for LMBs that is made using a crosslinked polymer matrix based on modified PEO (m-PEO). The m-PEO is synthesized by introducing methacrylate functionalities (crosslinkable groups) to end chains of regular PEO. The GPE is prepared by swelling the m-PEO matrix by $LiPF_6$ and carbonate solvents. At ambient temperature, Li|LFP cells with the GPE display an initial specific capacity value of approximately 130 mAh g^{-1} at 2C charge/discharge rate with ~70% capacity retention after 1000 cycles and around 99% CE. This superior electrochemical performance is attributed to the uniform, nondendritic growth of Li in the GPE as observed by o*perando* optical microscopy and scanning electron microscopy (SEM). Using cryogenic transmission electron microscopy (cryo-TEM) coupled with energy dispersive X-ray spectroscopy (EDS) and X-ray photon spectroscopy (XPS) characterization, detailed structure and chemistry of the SEI formed in the GPE and the liquid electrolyte is explored. To best of our knowledge, our work provides the first study on unveiling structure and chemistry of the SEI layer formed in GPEs by cryo-TEM, and the first report on direct visualization of electrochemical deposition of Li in GPEs by *operando* optical/light microscopy. The critical role of LiF in improving the electrochemical performance is supported by density functional theory (DFT) calculations.

2. Experimental section

2.1. Materials

Polyethylene oxide (PEO) with molecular weight of 20,000 g/mol, diethyl ether, anhydrous dimethyl carbonate (DMC), polyvinylidene fluoride (PVdF) with molecular weight of 534,000 g/mol, and N-Methyl-2-pyrrolidone (NMP) are purchased from Fisher Scientific. Trimethylamine (TEA), methacrylic anhydride (MA), dichloromethane (DCM), deuterated chloroform (CD_3Cl) with 0.3 wt% tetramethylsilane (TMS), liquid electrolyte of 1 M $LiPF_6$ in 1:1 v/v% ethylene carbonate/diethyl carbonate (EC/DEC) are purchased from Sigma-Aldrich. Lithium disk (Li, 0.3 mm thickness) and super-P carbon black (+99%) are purchased from Alfa Aesar, lithium iron phosphate (LFP) is purchased from MTI (USA), and Celgard® 2500 membrane battery separator (25 μm thickness) is purchased from Celgard.

2.2. Gel polymer electrolyte (GPE) preparation

PEO (10 g, 0.5 mmol) is dissolved in 20 ml DCM at ambient temperature and TEA (0.112 g, 1.1 mmol) is slowly added to the mixture. Then, MA (0.17 g, 1.1 mmol) is slowly added, and the resulting mixture is stirred for at least 24 hours. Afterwards, the m-PEO, which is a telechelic polymer with two polymerizable methacrylate groups, is isolated by precipitating in at least 10-folds diethyl ether. The isolated polymer is redissolved in DCM and reprecipitated in diethyl ether for at least three times to remove impurities and dried under vacuum at ambient temperature. It is worthy to mention that the methacrylate functionality is chosen due to its many advantages including facile and fast polymerization kinetic, insensitivity to air and moisture, stability and durability. MA is chosen as methacrylate functionality precursor due to low cost, nontoxicity, facile and efficient reaction with alcoholic groups. TEA is also used as base to deprotonate alcoholic functionality (OH) of the PEO and generating strong nucleophile to react with MA, thus enhancing the kinetic and efficiency of the PEO methacrylation. The crosslinked m-PEO polymer matrix or film is made by dissolving m-PEO in DMC and casting the resulting viscous solution into a polytetrafluoroethylene (PTFE) petri dish, followed by a chemical crosslinking under UV light (UV-lamp Model B100AP, 360 nm wavelength, 100 mW/cm^2 power, Black-Ray) for up to 10 minutes. The GPE is prepared by adding the conventional liquid electrolyte (1 M $LiPF_6$ in EC/DEC) to the crosslinked m-PEO film (circular disk) in a sealed glass vial at ambient temperature. Amount of the liquid electrolyte incorporated into the GPE is adjusted to keep the molar ratio of ethylene oxide to Li ions (EO:Li) equal to 20. For instance, 1 ml of the liquid electrolyte, which contains ~0.153 g (1 mmol) of $LiPF_6$ salt, is added to 1 gr (0.05 mmol) of the crosslinked m-PEO polymer film. The prepared GPE is stored in an Ar-filled glovebox.

2.3. Cell design

Electrochemical cells for *operando* optical/light microscopy experiments are prepared by sandwiching the GPE or the liquid electrolyte between two symmetric Li foils in sealed quartz cuvette cells. A constant current density of 5 mA cm^{-2} is applied to the cells using Gamry 600 Potentiostat/Galvanostat. Long-term stability test of the GPE or the liquid electrolyte against Li metal anode is performed using Li|Li coin cells. Li|LFP coin cells are prepared by sandwiching the GPE or the liquid electrolyte between a Li disk (anode electrode) and LFP (cathode electrode). To prepare the LFP cathode, a homogenous slurry consisting of 70 wt.% LFP, 15 wt.% Super-P carbon black, and 15 wt.% PVdF in NMP solvent is casted onto aluminum foil (current collector) by a doctor blade coating machine. The resulting film is dried at 60 °C for 1 hour and then 80 °C for 24 hours under vacuum and cut into circular disks using a punch machine. Mass load of the active material in the LFP cathode is around 2 mg cm^{-2}. 2032 coin-type cells are assembled in the glovebox.

2.4. General characterization

NMR is performed on a Bruker Avance 500 NMR spectrometer. Differential scanning calorimetry (DSC) is performed on TA Instruments DSC Q2000 at temperature range of -90°C to 100°C (±0.1% precision) with heating rate of 10°C/min. Alumina pans are used for both of sample and reference. TGA test is performed on TA Instruments Q5000 (±0.1% precision) at temperature range of 25°C to 600°C with heating rate of 10°C/min. Fourier transform infrared (FT-IR) spectroscopy is performed on Bruker LUMOS FTIR microscope. Tensile test is performed on Zwick-Roell zwickiLine Z0.5 instrument. A specimen with 8.75 mm width and 0.75 mm thickness is tested using a tensile test speed of 25% initial thickness/min. Swelling test is performed to measure the degree of crosslinking (gel content) of the crosslinked m-PEO film using acetonitrile solvent. The gel content is calculated using the equation $D = (m/m_0) \times 100$, where m_0 and m are the initial mass of the crosslinked polymer film and the final mass of the crosslinked polymer film after solvent removal (dried sample). *Operando* optical/light microscopy is performed on Nikon optical microscope. A constant current density of 5 mA cm^{-2} is applied to the Li|Li cuvette cells. A flexible and inert spacer is used between the GPE and Li foils to ensure a good electrode/electrolyte interfacial contact. SEM images are collected using JEOL JSM-IT500HR FESEM microscope operated at an accelerating voltage of 5 kV. The Li disk containing electrochemically deposited Li is prepared for SEM characterization by disassembling the symmetric Li|Li cuvette cells or the symmetric Li|Li coin cells inside the glovebox, followed by washing the electrode using 1,3-dioxolane to remove

residual electrolyte. Dried samples are sealed in hermetic vials inside the glovebox and are transferred for SEM characterization. XPS is performed on Thermo Scientific ESCALAB 250Xi. XPS spectra are collected using a monochromatized Al Kα radiation under a base pressure of 10^{-9} Torr. To avoid exposing the samples to moisture and air, samples are first loaded into an air-free XPS chamber and then transferred inside the XPS spectrometer. Survey scans are performed with a step size of 1.0 eV, and high-resolution scans with 0.1 eV resolution are collected for lithium (Li) 1s, carbon (C) 1s, oxygen (O) 1s, fluorine (F) 1s, and phosphorous (P) 2p regions. Cryo-TEM images are recorded on JEOL ARM200CF TEM, equipped with a Gatan Oneview camera operated at 200 kV. Li is electrochemically deposited onto a carbon-coated Cu grid placed between the electrolyte and Cu foil within Li|Cu coin cells. A constant current density of 0.5 mA cm^{-2} is applied. After Li electrodeposition, the coin cells are disassembled in the glovebox, TEM grid is detached and rinsed with 1,3-dioxolane to remove residual electrolyte. Then, the Li metal deposited Cu grid is placed in a cryo grid box, and the grid box is placed in a vial container and sealed in the glovebox. The TEM grid is immersed into liquid nitrogen and then mounted onto a single-tilt Gatan 626 liquid nitrogen cryo-holder (Gatan, USA) using a cryo-transfer workstation. The cryotransfer station is used to ensure that the specimen is under cryogenic and inert nitrogen environment throughout the transfer process to keep the specimen in its native state.

2.5. Electrochemical test

Electrochemical tests are performed on BioLogic VMP3 potentiostat/galvanostat and Neware CT-4008 battery cycler. All electrochemical tests are performed at ambient temperature (~20°C), unless it is stated. To measure Li ion conductivity, the GPE or the liquid electrolyte are sandwiched between two symmetric stainless-steel discs as blocking electrodes and sealed in CR2032 coin cells. A PTFE ring with 14 mm inner diameter and 0.5 mm thickness is used as a separator between the stainless-steel electrodes (the opening of the PTFE ring is filled with the liquid electrolyte or the GPE). The electrochemical impedance spectroscopy (EIS) data is collected in the frequency range of 1 MHz to 100 mHz in a temperature range from 20 °C to 60 °C, regulated by a climate chamber (Binder, Tuttlingen, Germany). The Li ion conductivity is calculated using the equation $\sigma = L/R_b \times S$, whereas σ is the Li ion conductivity ($S\ cm^{-1}$), R_b is the bulk electrolyte resistance (Ω), L is the thickness of the electrolyte or separator (*cm*), and S is the surface area of the electrolyte in contact with the stainless-steel disk. Electrochemical stability window of the electrolytes is evaluated by linear sweep voltammetry (LSV) using a stainless-steel disc as the working electrode and a Li disc as the counter and reference electrode. The voltammograms are recorded between 2 V and 6 V (vs. Li|Li^+) at a sweep rate of 0.5 mV s^{-1}. The long-term stability of the electrolytes against Li metal are measured on symmetric Li|Li cells under constant current density of 0.5 $mAcm^{-2}$ and 1.0 $mAcm^{-2}$, with a 30 min platting/stripping for each cycle. Long-term cycle performance of LMBs with the GPE and the liquid electrolyte are tested at 1C and 2C charge/discharge rates (1C= 160 mA g^{-1}) with a voltage cut-off of 4.2 V and 2.5 V for charging and discharging, respectively. The rate performance of the GPE and the standard liquid electrolyte at different charge/discharge rate is also explored. Li|Li and Li|LFP cells with the GPE or the liquid electrolyte (~100 μL) are assembled in standard 2032 coin-type cells.

2.6. Computational details

DFT calculations are performed using the Vienna Ab Initio Simulations Package (VASP) [22] code employing the generalized-gradient approximation (GGA) [23] using the PBE (Perdew, Burke, and Ernzerhof) [24] functional to account for the exchange-correlation effects. For systems with an even number of electrons non-spin polarized calculations, and for systems with an odd number of electrons unrestricted spin-polarized calculations are performed. Li ions migration paths and barriers are determined using the linear nudged-elastic-band (NEB) method as implemented in VASP code. For all calculations, a cutoff energy of 450 eV is used. The further increase of cutoff energy to 500 eV led to the change of the total energy of less than 0.01 eV. All structural optimizations are carried out until the forces, acting on atoms, are below 0.01 eV/Å. The criterion for energy change is set to 0.1 eV. The ground-state lattice constants of LiF are first calculated. Then, using a slab method, the (111) surface energy is calculated. The k-point samplings are set based on the geometry of each structure for surface structure optimization, with one k-point in the surface normal direction defined with at least 15 Å vacuum region and same number of in-plane k-points as in the bulk calculations. The presence of EC/DEC solvents influences Li adsorption as well as other adsorbate structures over the LiF surface. To consider the influence of the solvent on the adsorption energies of Li intermediates, we have used the implicit solvent (polarized continuum) model as implemented in the VASPsol. EC/DEC electrolyte is considered as a medium with the dielectric constant of 32.

3. Results and discussion

Polymer crosslinking is a typical method of making free-standing polymeric gels [19,20]. Chemical crosslinking is also shown to induce improvement in dimensional stability and modulus of polymer electrolytes [19,20]. We employed a one-step, facile methacrylation process to modify the regular PEO and make it self-crosslinkable (Fig. 1a). The m-PEO has ability to polymerize and form chemical crosslinks at the polymer end chains, thus preserving the original polymer chain length and mobility of the regular PEO. Proton NMR (^{1}H NMR) is used for chemical characterization of the m-PEO and the regular PEO. As displayed in Fig. S1, the regular PEO shows a sharp and wide signal ~3.5-4 ppm related to ethylene (-CH_2-CH_2-) protons of the PEO backbone. Beside this signal, m-PEO also shows new signals at ~1.5 ppm and ~5.5-6.0 ppm related to CH_3 and CH protons, respectively, of the introduced methacrylate groups. A photograph of the crosslinked m-PEO polymer matrix punched into a circular disk is shown in Fig. 1b. A photograph of the GPE made by swelling the crosslinked m-PEO matrix using the conventional liquid electrolytes (1 M $LiPF_6$ in EC/DEC) is shown in Fig. 1c. We have also performed ^{1}H NMR to measure the gel content or degree of crosslinking of m-PEO matrix within the GPE (Fig. S2). This is done by calculating number of the unpolymerized m-PEO or remaining ethylenic or vinyl protons (CH) in the GPE. Due to a small fraction of ethylenic protons versus polymer backbone protons upon chemical crosslinking, a magnified region related to the ethylenic protons is also shown as inset. By integrating the area under the peak of an ethylenic proton (CH) with regards to the peak of methyl protons (CH_3) of the methacrylate functionality or the polymer backbone protons (-CH_2-CH_2-), ~5% of the ethylenic bonds is found to be remained unpolymerized after the crosslinking (degree of crosslinking is ~95%). A similar degree of crosslinking for the m-PEO film is obtained by the swelling test.

DSC is performed to assess the effect of chemical modification and crosslinking on original properties of the unmodified PEO. The DSC curves indicating melting temperature (T_m) and crystallization temperature (T_c) of the regular PEO and the crosslinked m-PEO film are shown in Fig. S3. The unmodified PEO shows T_m~ 61 °C during heating cycle and T_c~ 42 °C during cooling cycle (Fig. S3a). These values are very similar for the crosslinked m-PEO film with T_m~ 58 °C and T_c~ 42 °C (Fig. S3b). This suggests that the polymer chain length and mobility of the regular PEO does no considerably change upon the chemical modification or crosslinking [25]. Fig. S3c shows DSC curve of the GPE at which no T_m or T_c can be detected, indicating that the polymer matrix is fully amorphous. The small peaks (T_m~ 15 °C and T_c~ -45 °C) can be attributed to the melting and crystallization of the EC/DEC carbonate solvents [26]. Thermal stability of the GPE is explored by TGA (Fig. S3d) and two major weight loss is observed. The first major weight loss (~53%) up to 250 °C can be attributed to evaporation/decomposition of the liquid electrolyte (Li salt and organic solvents) and the second major

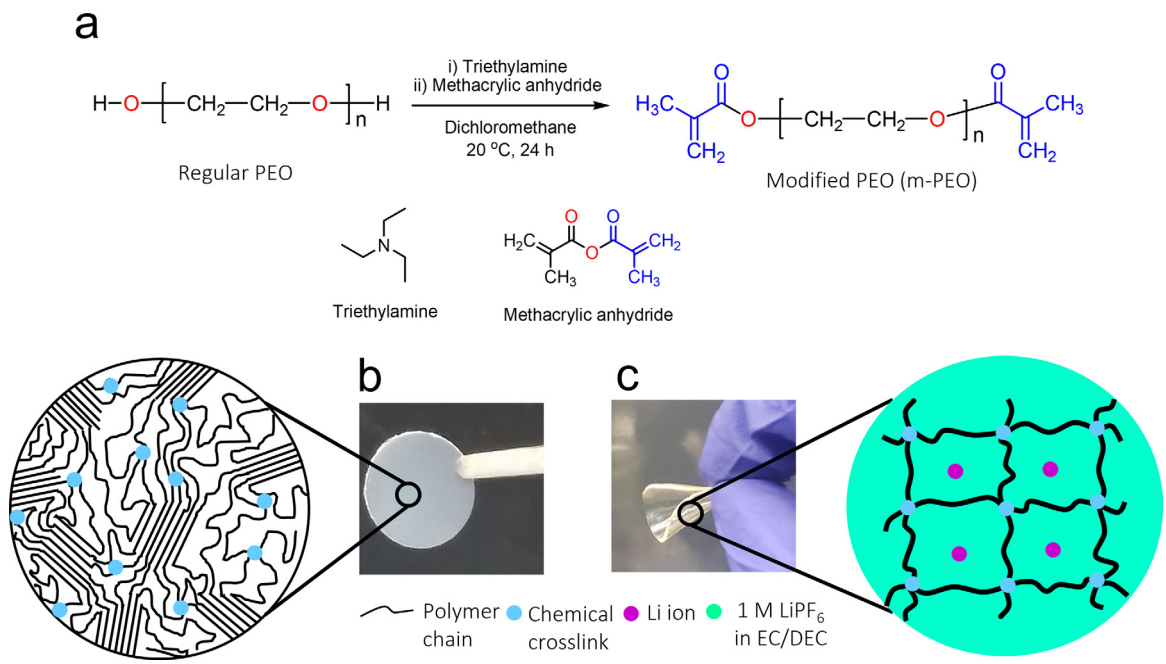

Fig. 1. The GPE preparation. (a) Synthesis of m-PEO by chemical modification (methacrylation) of the regular PEO. (b) A photograph of the semi-crystalline, crosslinked m-PEO polymer film and schematic illustration of its molecular structure. (c) A photograph of the GPE made by swelling of the crosslinked m-PEO matrix by the conventional liquid electrolyte (1 M $LiPF_6$ in EC/DEC) and schematic illustration of its molecular structure.

weight loss (~47%) at ~400 °C can be attributed to thermal decomposition of the m-PEO polymer matrix. A similar decomposition behavior for 1 M $LiPF_6$ in EC/DEC and PEO/PEG is reported elsewhere [19,27,28]. Furthermore, the TGA curve indicates that the weight loss related to the liquid electrolyte is slightly larger than the m-PEO matrix. This is consistent with the designed GPE composition made of 1 ml (~1.2 g) of the liquid electrolyte versus 1 g of the m-PEO matrix. FT-IR is also employed to characterize the chemical composition and structure of the regular PEO before and after the chemical modification and crosslinking (Fig. S4). PEO shows several major signals around 841 cm^{-1} (C-O-C bond), 1097 cm^{-1} (C-O bond), 1340 cm^{-1} (CH_2 bond), and 2880 cm^{-1} (C-H bond) [29–31]. The major difference between regular PEO and m-PEO is the presence of methacrylate functionality, $H_2C{=}C(CH_3)$-C=O-. Hence, appearance of new signals around 1641 cm^{-1} and 1718 cm^{-1} can be attributed to the ethylene (C=C) and carbonyl (C=O) bonds introduced upon methacrylation of the PEO [30]. Furthermore, there is a small shift in position of C=O bond of the crosslinked m-PEO compared to uncrosslinked m-PEO. This can be attributed to conversion of unsaturated C=C bonds into saturated C-C bonds upon the chemical crosslinking, leading to a change in electronegativity of the neighboring group of the C=O bond. It is important to mention that relatively weak signals observed for C=C and C=O bonds is because m-PEO consists of a small fraction of methacrylate functionality with respect to the polymer backbone. FT-IR spectra of the GPE is also presented in Fig. S5. Beside signals related to the crosslinked m-PEO film, some new signals appear upon the liquid electrolyte addition which can be ascribed to the $LiPF_6$ salt and EC/DEC organic solvents [32,33]. A tensile mechanical test is also performed to measure mechanical property of the developed GPE (Fig. S6). The stress-strain curve indicates that the GPE posseses an elastic nature with high strechablility and resistance against fracture. Electrochemical stability window of the GPE is measured by LSV and is compared with the liquid electrolyte (Fig. S7). The liquid electrolyte exhibits an anodic oxidation onset around 3.8 V (vs. $Li|Li^+$), while the GPE exhibits an anodic oxidation onset around 4.2 V (vs. $Li|Li^+$). This value is beyond the cut-off voltage of 2.5 V (for discharge) and 3.8 V (for charge) of L Li|LFP batteries. Li ion conductivity of the GPE and the liquid electrolyte is also measured at different temperatures, and the corresponding results are shown in Fig. S8. According to the findings, the GPE shows an ion conductivity of 1.5 mS cm^{-1} at ambient temperature, which is close to that for the liquid electrolyte (8.1 mS cm^{-1}).

Fig. 2a and b display time-lapse snapshots of the electrochemical deposition of Li in the liquid electrolyte and the GPE, respectively, captured by *operando* light microscopy. An uneven nucleation and growth of Li electrodeposits with mossy structure occur for the liquid electrolyte. Unevenness and heterogeneity in Li electrodeposition are well-known for liquid electrolytes with carbonate solvents and is correlated to unregulated Li ions flux [12]. It is important to note that this topology can result in constant consumption of organic solvents, leading to constant formation and accumulation of the SEI layer which can result in capacity instability or loss and poor CE in LMBs [34]. In contrast to the liquid electrolyte, a uniform and even Li platting is observed for the GPE which can be ascribed to regulation of Li ions flux by PEO-based polymer matrix. The cuvette cells are disassembled after the experiment and the topology of the deposited Li particles is characterized by SEM (Fig. 2c and d). The SEM images further indicates microscopic homogeneity of the Li deposition for the GPE in contrast to the heterogeneous Li deposition for the liquid electrolyte.

To further explore the Li platting behavior, topology and morphology of the electrochemically deposited Li for Li|Li cells with the GPE and the liquid electrolyte is investigated by SEM (Fig. 3). Consistent with *operando* light microscopy results, Li electrodeposition is uneven and dendritic in the liquid electrolyte (Fig. 3a and b). On the other hand, a uniform and dendrite-free Li electrodeposition is observed in the GPE (Fig. 3c and d). The high surface area of dendritic Li significantly facilitates side reactions between the deposited Li and electrolyte. This can cause in constant consumption of the electrolyte, formation of a thick SEI layer with poor Li ion conductivity, and formation of electrically isolated or “dead/inactive” Li (Fig. 3e). All of these incidents lead to increasing battery cell impedance, a low CE, capacity loss and short lifespan in LMBs. It is known that morphology and structure of electrochemically deposited Li are related to the deposition time, applied current density, and electrolyte chemistry [35]. Since a similar deposition time and applied current density is employed for the Li platting in both the liquid electrolyte and the polymer electrolyte, electrolyte

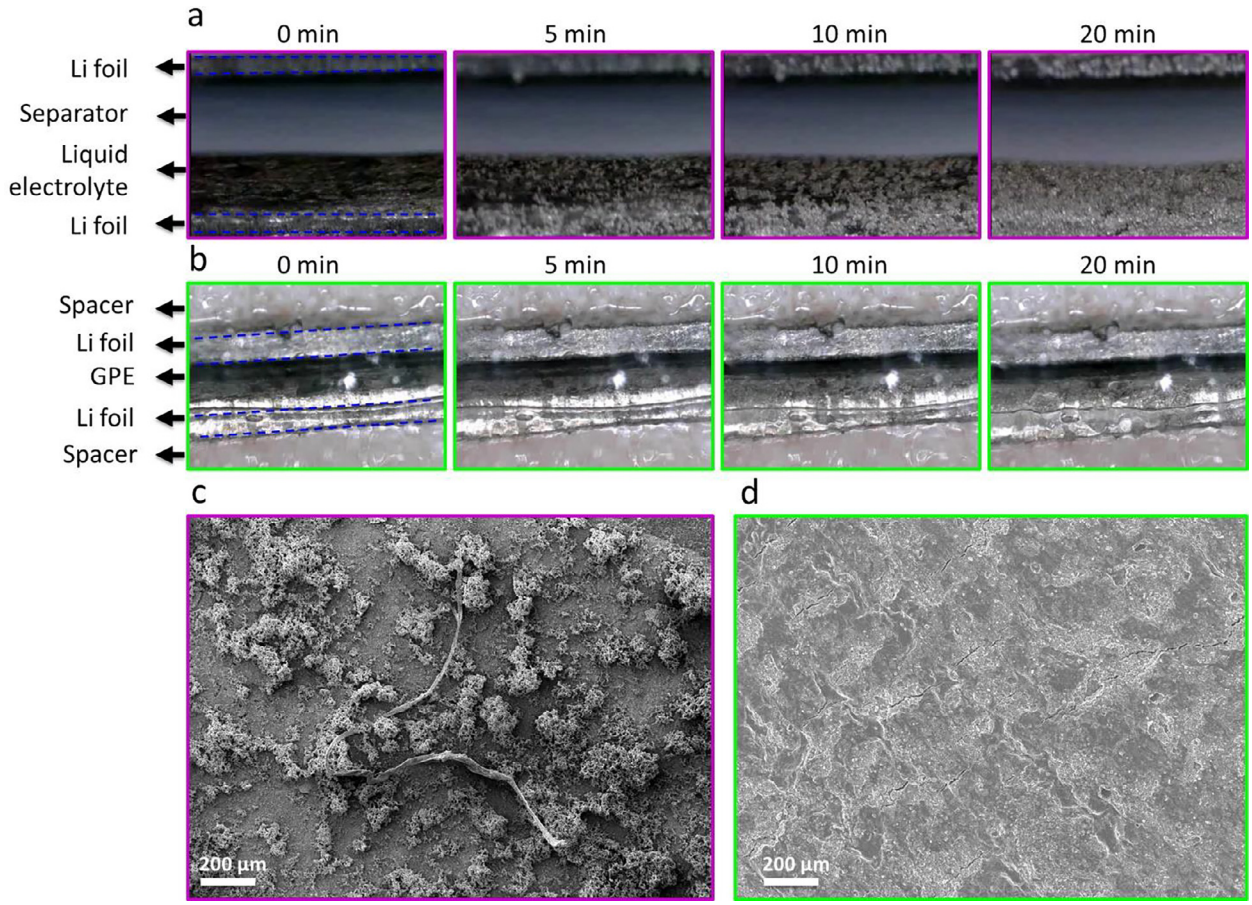

Fig. 2. Time-lapse snapshots of electrochemical deposition of Li in the liquid electrolyte (a) and the GPE (b) after 0, 5, 10, and 20 min of Li deposition captured by *operando* light microscopy. SEM images of the bottom Li electrode surface after 20 min of Li plating in the liquid electrolyte (c) and the GPE (d).

chemistry is playing the major role in controlling topology or morphology of the deposited Li. Therefore, it can be concluded that the uniform Li platting observed for the GPE can be correlated to regulation of Li ions flux by the PEO-based polymer matrix. The formation of pits on Li electrode surface (Fig. S9) after five cycles of Li platting/stripping in the liquid electrolyte also indicates the presence of Li ions gradient on the Li electrode and lack of Li ions regulation by the conventional liquid electrolyte. Based on the space-charge theory, the formation and evolution of Li dendrites is related to Li ions transport driven by the electric field on the Li anode. It is well-known that PEO own a high Li ion solvating power, enabling Li ions regulation and uniform distribution within the polymer electrolyte [11,17,34,36]. Moreover, PEO-based polymer electrolytes intrinsically own higher Li salt dissociation rate than liquid electrolytes, indicated by higher Li ion transference number. This can result in stronger electrolyte-Li ions complexation and more uniform distribution of Li ions in the polymer electrolytes [11,36]. EDS elemental mapping (Fig. S10) further indicates a uniform distribution of C, O, F, P elements on the surface of the electrochemically deposited Li particles in the GPE.

It is also widely believed that the morphology of electrochemically deposited Li is closely dependent on structure and composition of the SEI layer [35]. Therefore, we have investigated the Li/GPE interface as well as Li/liquid electrolyte interface at nanoscale by cryo-TEM. Fig. S11 shows voltage profiles for Li metal electrodeposition in Li|Cu cells with the liquid electrolyte and the GPE. A voltage drop at the initial stage of the Li deposition followed by a flat plateau are observed, corresponding to the nucleation region (the nucleation overpotential) and the growth region (the plateau overpotential), respectively [37]. Magnitude of the nucleation overpotential defines the nucleation barrier between the Li and Cu for the electrodeposition. Figs. 4 and 5 exhibit morphology, crystalline structure and chemistry of the electrochemically deposited Li in the liquid electrolyte and the GPE, respectively, after the first discharge acquired by cryo-TEM. Similar to the SEM results, low-magnification TEM images (Figs. 4a and 5a) show a dendritic Li growth in the liquid electrolyte versus a nondendritic Li growth in the GPE. The SEI layer formed in the liquid electrolyte show a mosaic-type nanostructure, whereas Li-based inorganic nanocrystals are embedded in an amorphous organic/polymeric matrix (Fig. 4b, Table S1 and S2) [35,38,39]. The SEI layer formed in the liquid electrolyte appears to be mostly amorphous which is consistent with the previous reports [35,37,40]. It is well-known that inorganic and organic decomposition products derived from the electrolyte (Tables S1 and S2) are precipitated and heterogeneously distributed throughout the SEI, forming a mosaic-type microphases containing both crystalline and amorphous phases [41]. It is also known that the SEI layer formed in carbonate solvents-based liquid electrolytes is typically uneven and thick mostly composed of amorphous organic/polymeric phase with a poor Li ion conductivity [35,39,42–44]. The presence of crystalline nanograins is also confirmed by selected area electron diffraction (SAED) pattern illustrated in Fig. 4c. High-resolution TEM (HRTEM) images are also captured to study detailed nanostructure and chemistry of the Li/liquid electrolyte interface. HRTEM images of the crystalline nanocrystals within the SEI film are identified to be LiOH, Li_2O and Li_2CO_3 (Fig. 4d-f). Lattice spacings of 4.4 Å, 2.66 Å and 4.2 Å are identified by HRTEM, which match well with (001), (111), and (110) planes of LiOH, Li_2O and Li_2CO_3, respectively. Moreover, the rings observed in the fast Fourier transform (FFT) patterns (Fig. 4g-i) of the high-resolution images suggest that the SEI layer is mostly rich in Li_2O and LiOH. This is found from calibrated

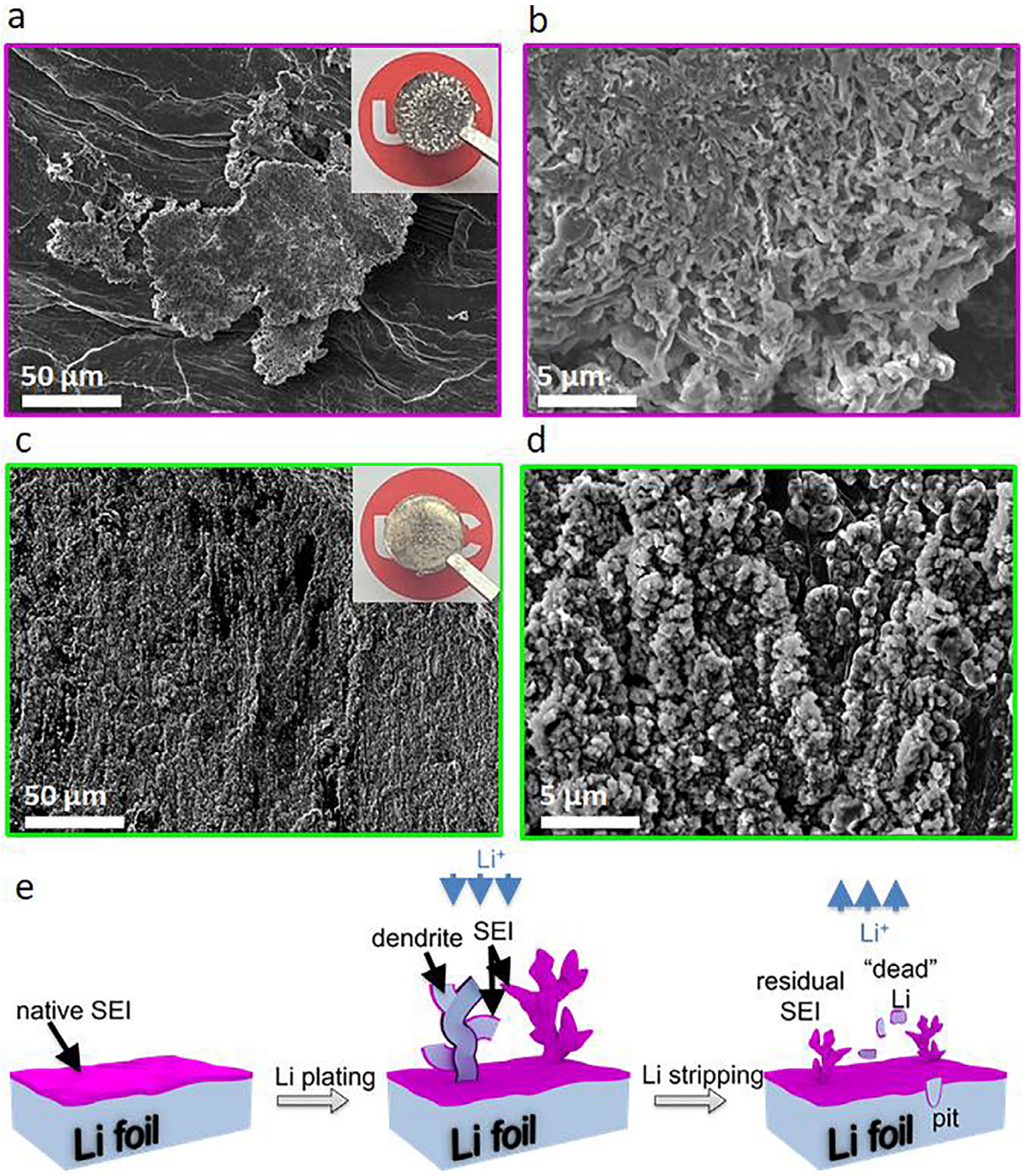

Fig. 3. SEM images at different magnifications of the Li electrode surface after five cycles of Li plating/stripping in the liquid electrolyte (a,b) and the GPE (c,d). The Li platting/stripping is performed under a constant current density of 0.5 mA cm^{-2} with 30 min platting/stripping for each cycle at ambient temperature. Insets in (a) and (c) show photographs of the Li electrode surface after five cycles of Li plating/stripping in the liquid electrolyte and the GPE, respectively. (e) Schematic illustration of the formation of excessively thick SEI layer and dead/inactive Li as result of dendritic Li growth in the liquid electrolyte.

interplanar spacings of 4.4 Å and 2.66 Å which match well with the (001) and (111) planes of LiOH and Li_2O, respectively.

The SEI layer formed in the GPE (Fig. 5b) also shows a mosaic-type structure where Li_2O, LiOH, Li_2CO_3, and LiF nanocrystals are embedded in an amorphous organic/polymeric phase. The presence of crystalline nanograins is also confirmed by SAED pattern (Fig. 5c). Particularly, the indexed crystal structures of Li_2CO_3, Li_2O, and LiF are presented in Fig. 5d-f. Using the FFT patterns (Fig. 5g-i), Li_2CO_3, Li_2O, and LiF crystals with d-spacings of 4.2 Å, 2.66 Å, and 2.32 Å, and lattices aligning along (110), (111), and (111), respectively, can be identified [37,41,45].

It worth to mention that in contrast to the SEI layer formed in the liquid electrolyte being mostly amorphous (Fig. 4b and c), the SEI layer formed in the GPE is highly rich in inorganic nanocrystals (Fig. 5b and c). It is well-known that nanocrystalline grains in the SEI layer facilitate fast Li ions transport through the amorphous organic/polymeric matrix [43]. Most of these ceramic-like nanocrystals (i.e., Li_2O, Li_2CO_3) are known to own low bulk Li ion conductivity, making the Li ions conduction pathways to mostly present at the nanocrystals-amorphous phase interface [39,40]. Many reports in the literature also experimentally demonstrate significant ionic conductivity enhancement when ceramic nanocrystals

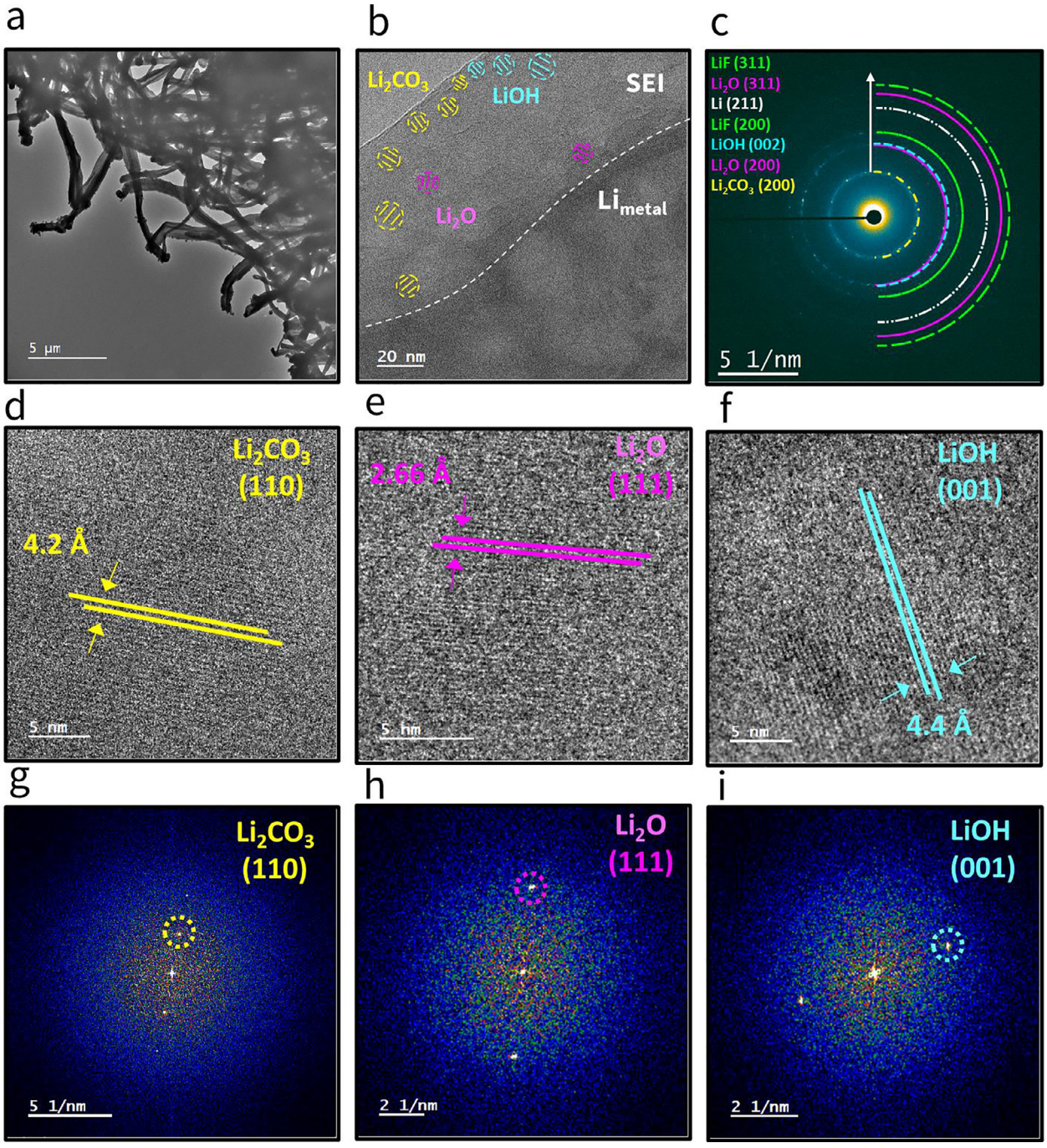

Fig. 4. Nanostructure of the electrochemically deposited Li in the liquid electrolyte (1 M $LiPF_6$ in EC/DEC). (a) A low magnification cryo-TEM image of the electrochemically deposited Li particles. (b) HRTEM image illustrating the nanoscale SEI layer with its structure and chemistry. (c) The corresponding SAED pattern of the Li particle. Representative HRTEM images and FFT patterns of Li_2CO_3 (d, g), Li_2O (e, h), and LiOH (f, i) in the SEI layer.

are dispersed within solid polymer electrolytes, a system very similar to the mosaic-type SEI [46,47]. A possible explanation could be a strong affinity between acidic groups on the nano-oxide or nano-hydroxide grains and Li salt anion in the electrolyte (PF_6^- in this case) [46]. This facilitates separation of the Li^+-PF_6^- ion pairs and allow rapid motion of Li ions at the polymer-ceramic interface. The importance of space-charge effects in facilitating ionic conduction at interface of heterostructure materials is shown previous studies [48]. We also found that the Li/GPE interface is rich in LiF, in a sharp contrast to the Li/liquid electrolyte interface. The HRTEM image of LiF exhibits a lattice spacing of 2.32 Å, which matches well with (111) plane of LiF [38]. According to the SAED pattern (Figs. 4c and 5c), the extent of LiF in the SEI formed in the GPE is significantly higher than that for the conventional liquid electrolyte of 1 M $LiPF_6$ in EC/DEC.

By employing scanning transmission electron microscopy (STEM) coupled with EDS under the cryogenic condition, the elemental distribution of C, O, F, and P is spatially mapped (Fig. 6a and b). A significant difference in the chemical composition can be identified for the SEI film formed in the GPE when compared to the conventional $LiPF_6$-EC-DEC liquid electrolyte. Quantitative analysis of the EDS data reveals that atomic ratio of C to O is higher in the SEI layer formed in the liquid electrolyte, further indicating a highly amorphous nature of the SEI layer.

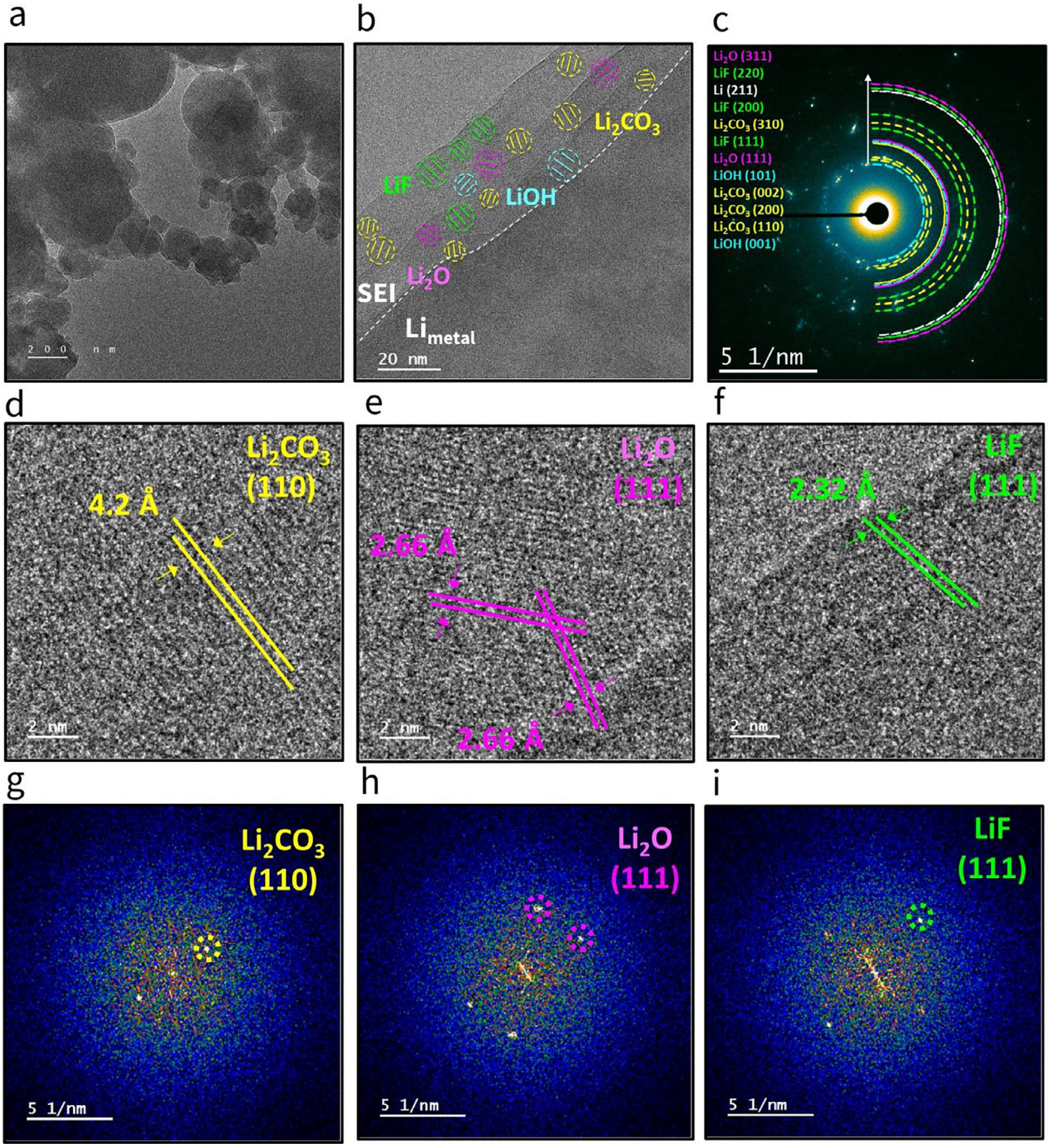

Fig. 5. Nanostructure of the electrochemically deposited Li in the GPE. (a) A low magnification cryo-TEM image of the electrochemically deposited Li particles. (b) HRTEM image illustrating a nanoscale SEI layer with its structure and chemistry. (c) The corresponding SAED pattern of the Li particle. Representative HRTEM images and FFT patterns of Li_2CO_3 (d, g), Li_2O (e, h), and LiF (f, i) in the SEI layer.

Since the organic/polymeric components of the SEI layer are degradation products of the organic solvents, the carbon content and the oxygen content are expected to be comparable in a region that is predominantly amorphous. Contrarily, a more crystalline SEI is observed at the Li/GPE interface. A highly crystalline SEI layer rich in crystalline grains of Li_2O, LiOH, and Li_2CO_3 is expected to have a higher content of oxygen than carbon. Consistent with the cryo-TEM images, the EDS results (Fig. 6a and b) also demonstrate that the Li/GPE interface contains higher LiF content compared to the Li/liquid electrolyte interface.

The Li|LFP cells with the GPE and the liquid electrolyte are disassembled after 100 charge/discharge cycles to characterize the surface of the Li metal electrode by XPS (Fig. 6c,d and Fig. S12). Based on the findings and consistent with the cryo-TEM results, both the Li/GPE interface and the Li/liquid electrolyte interface are composed of LiOH, Li_2O, Li_2CO_3 and LiF. The signals related to the amorphous organic/polymeric phase can also be observed in C 1s and O 1s spectrums. It is also important to mention that similar to the cryo-TEM results, the SEI film formed in the GPE is richer in LiF compared to the SEI film formed in the liquid electrolyte. The LiF-rich SEI layer formed in PEO-based polymer electrolytes is also shown by cryo-TEM and XPS studies elsewhere [38,39].

A schematic illustration of the electrochemically deposited Li morphology, and structure and chemistry of the SEI layer formed in the GPE

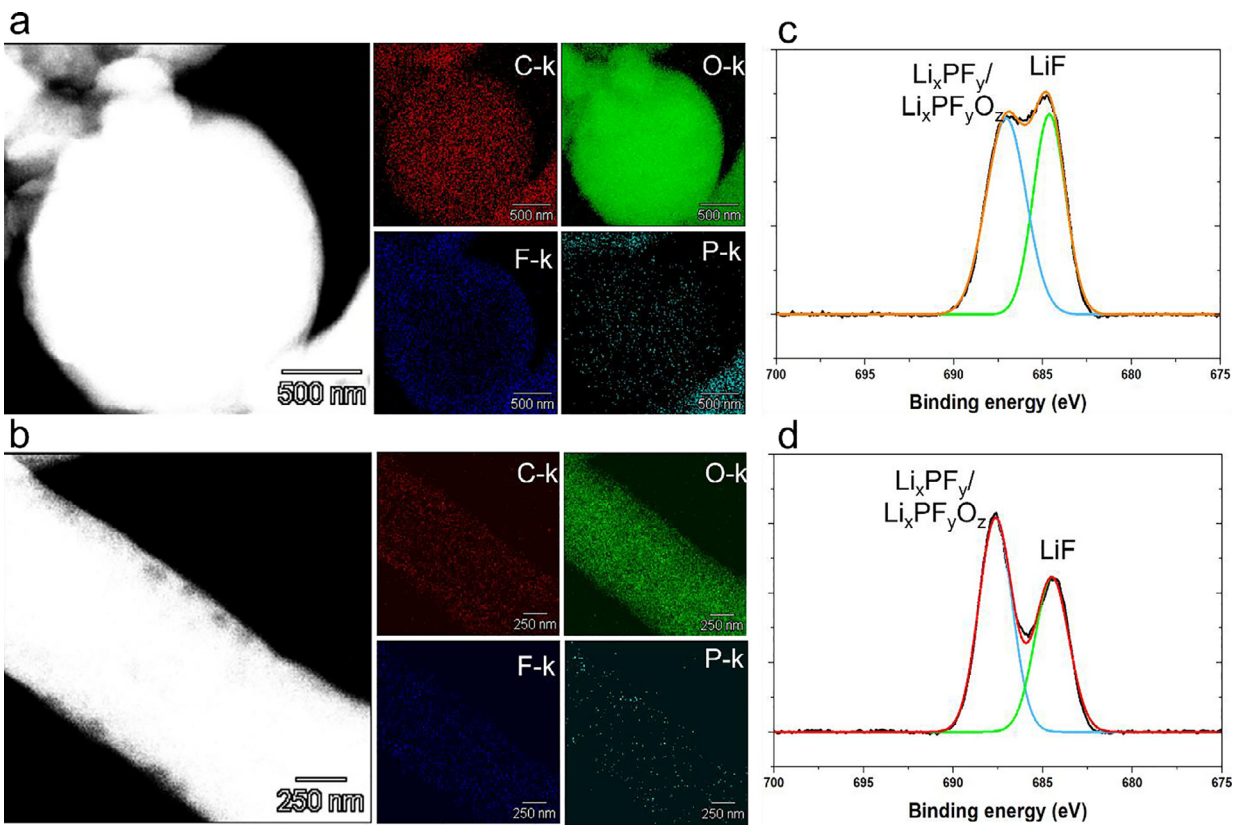

Fig. 6. Surface elemental analysis of the electrochemically deposited Li by EDS. (a) High-angle annular dark-field STEM (HAADF-STEM) image of the electrochemically deposited Li in the GPE and the corresponding elemental maps of C, O, F and P. (b) HAADF-STEM image of the electrochemically deposited Li in the conventional liquid electrolyte (1 M $LiPF_6$ in EC/DEC) and the corresponding elemental maps of C, O, F and P. XPS analysis of the Li electrode surface obtained from Li|LFP cells with the GPE and the liquid electrolyte after 100 cycles at 1C charge/discharge rate. LiF identification in the SEI layer formed in the GPE (c) and the liquid electrolyte (d).

and the liquid electrolyte is shown in Fig. 7. Due to numerous advantages including low electronic conductivity, high electrochemical stability, high mechanical modulus, low energy barrier (~0.19 eV) for Li ions surface conductivity and diffusion, LiF is one of the most favorable component in the SEI layer [39,49]. Enhancement in electrochemical performance of LMBs via LiF-rich interfaces is widely reported in previous studies [38,39,43,45]. Low energy barrier for Li ions diffusion at LiF surface promotes Li ions migration along LiF-surface, regulating the homogeneous of Li ions flux. While bulk LiF is a poor Li ion conductor, its interfacing with other crystalline grains in the SEI (e.g. Li_2O, Li_2CO_3) at the nano-scale is shown to possess high Li ion conductivity [39,40]. Ramasubramanian et al. [40] showed that the fastest Li ion diffusion rate occurs for the heterogeneous LiF/Li_2O grain boundary. Similarly, Zhang et al. [50] demonstrated that the interface formed between Li_2CO_3 and LiF particles can promote ionic carriers concentration. Nanostructured LiF in the SEI is also reported to induce uniform diffusion field gradient in Li metal electrode [35].

Galvanostatic Li plating/stripping for the Li|Li cells with the GPE and the liquid electrolyte is performed to determine stability of the electrolytes against Li metal anode. Measurements are carried out under current densities of 0.5 mA cm^{-2} and 1.0 mA cm^{-2} with 30 min of Li plating/stripping at ambient temperature (~20 °C). Voltage profile for the Li|Li cells with the GPE (**Fig. 8**a and Fig. S13) shows a smaller voltage polarization in comparison to the Li|Li cells with the liquid electrolyte (Fig. 8a and Fig. S13). This can indicate a higher Li ion conductivity of the Li/GPE interface enabled by the LiF-rich SEI compared to the Li/liquid electrolyte interface. Moreover, the stable nature of the Li/GPE interface leads to a long lifespan of Li plating/stripping cycles (up to 800 cycles). In a sharp contrast, unstable nature of the Li/liquid electrolyte interface leads to a short lifespan of the symmetric Li|Li cell. In particular, a constant increase in the polarization over cycling is observed in the case of the Li/liquid electrolyte, which is followed by the cell shorting, as evident form sudden drop in the potential (Fig. 8a). This can be attributed to the dendritic morphology of the electrochemically deposited Li in the liquid electrolyte, resulting in constant degradation of the organic solvents, leading to thickening and build-up of the SEI film (Fig. 3e) [51]. The numerical studies have shown that the overpotential of Li metal anode contributes mostly to the voltage shift at initial stages, that is due to dynamic evolution of the surface morphology of Li deposits [52]. However, during later cycles, growth of inactive/dead Li proceeds, creating a porous Li deposits and a tortuous pathway for Li ions transport across electrode/electrolyte interface (Fig. 3e) [51]. This can decrease the local ionic diffusion coefficient, and suppress ohmic transport in the electrolyte by the inactive/dead Li layer [53]. With continued cycling, the inactive/dead Li layer becomes more tortuous and denser, causing in a further decrease in the effective ionic conductivity and diffusion coefficient. It is also known that aggressive Li dendrites formed during cycling can penetrate through the separator leading to an internal short-circuit in LMBs [35].

The electrochemical performance at different C-rates for the LMBs with the GPE and the liquid electrolyte is shown in Fig. S14. Cycle performance of the LMBs with the GPE and the liquid electrolyte at 1C and 2C charge/discharge rates is also explored. According to the charge/discharge profiles (Fig. S15) and the cycle performance results (Fig. 8b), the LMB with the GPE indicate a low polarization with a specific capacity of ~140 mAh g^{-1} and ~70% capacity retention after 1000 cycles at 1C charge/discharge rate. In a sharp contrast, the LMB with the liquid electrolyte indicate a relatively large voltage polarization with a

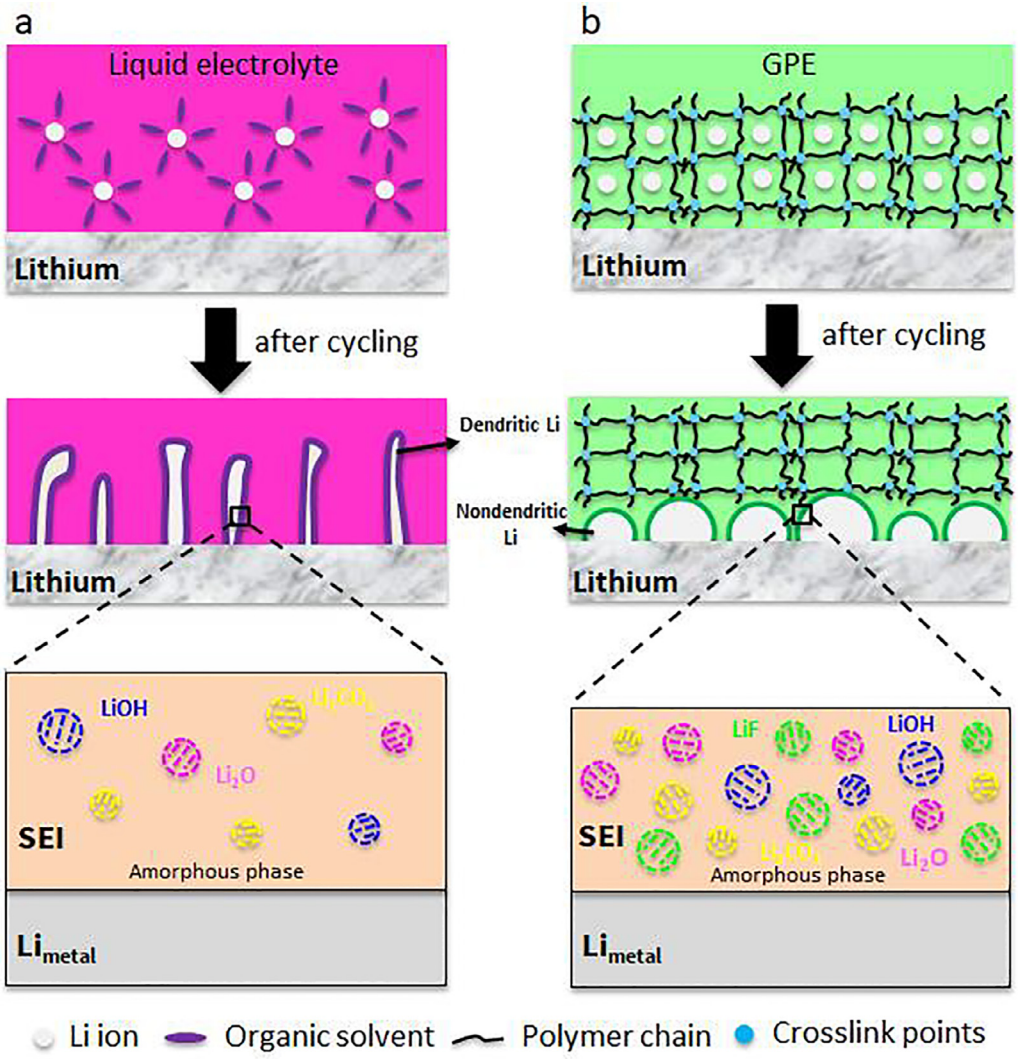

Fig. 7. Schematic illustration of the electrochemically deposited Li with the corresponding SEI layer formed in the liquid electrolyte (a) and the GPE (b).

specific capacity of ~125 mAh g^{-1} and less than 40% capacity retention after 1000 cycles at 1C charge/discharge rate. Similar results are observed for the LMBs cycled at 2C charge/discharge rate (Fig. 8c and Fig. S16). In particular, the Li|LFP cells with the GPE and the liquid electrolyte show specific capacities of ~130 mAh g^{-1} and ~110 mAh g^{-1}, respectively, at 2C charge/discharge rate. While the LMB with the GPE shows ~70% capacity retention after 1000 cycles, the capacity retention for the LMB with the liquid electrolyte is only ~30%. The long lifespan and the high capacity retention rate observed for LMBs with the developed GPE in this work also exceeds the lifespan and capacity retention rate of LMBs with PEO-based GPEs reported in the literature (Table S3) [13,17,18,20]. Capacity fluctuations observed for the LMBs could be due to ambient temperature fluctuations [54], SEI evolution and irreversible interface destruction [55,56], defective Li ion transport [57], mechanical strength of the electrolyte [57], instability of the Li anode [58].

The superior cycle performance of the LMBs with the GPE can be correlated to the Li ions regulation via oxygen atoms of the m-PEO within the GPE matrix, leading to uniform Li platting/stripping [11,34,36]. As discussed earlier, PEO is shown to effectively regulate Li ions transport which can lead to uniform and nondendritic Li plating [34,36]. Assegie et al. [11] showed that coating a thin layer of PEO onto Cu foil can lead to a uniform Li deposition in the liquid electrolyte. Through hosting Li ions and regulating its inevitable reaction with the electrolyte, the PEO layer also results in high compatibility of electrode–electrolyte interface, promoting the formation of a thin and robust SEI layer. The modified electrode exhibited stable Li cycling with >99% CE over 200 cycles and low voltage polarization at 0.5 mA cm^{-2} current density. Besides, the superior electrochemical performance of the GPE versus the conventional liquid electrolyte can be due to the sharp difference in the SEI structure and chemistry. The presence of LiF-rich SEI promote a dense and smooth Li deposition, facilitate Li ions transport and enable uniform Li platting. Indeed, a more crystalline and LiF-rich interface for the GPE enables a surface-growth of electrochemically deposited Li and thus, suppress the formation of Li dendrites. As a result, the LMBs with the GPE exhibit a longer lifespan and higher CE compared to the LMBs with the $LiPF_6$-EC-DEC liquid electrolyte.

To further analyze the Li/electrolyte interface, the impedance behavior before cycling for the LMBs with the GPE and the liquid electrolyte is studied (Fig. S17). The simulated graphs are plotted using the closest values of the equivalent circuits with regards to the corresponding experiment. The equivalent electrical circuit is a useful technique to distinguish resistive behavior of battery components at various frequencies [59]. As illustrated in Fig. S17, two different time-constants are observed for both the GPE and the liquid electrolyte: one for the electrode/electrolyte interface (SEI layer, cathode electrolyte interphase (CEI), and charge-transfer resistive at Li/electrolyte or electrolyte/LFP interfaces) and the other one for a semi-infinite diffusion [59,60]. It

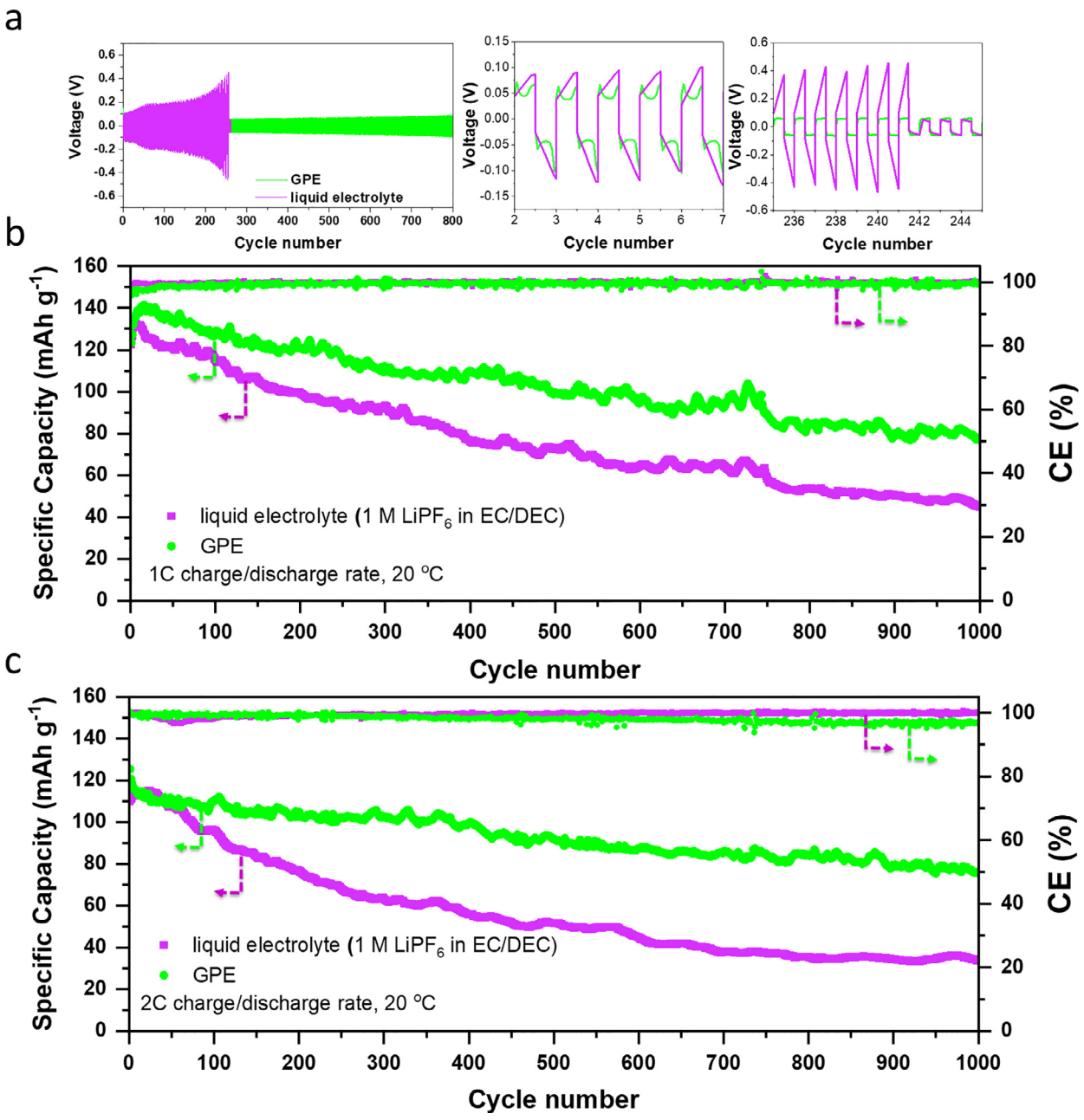

Fig. 8. Electrochemical cycle performance of LMBs and Li|Li cells with the GPE and the liquid electrolyte (1 M $LiPF_6$ in EC/DEC). (a) Overpotential profile of the Li|Li cells with the GPE and the liquid electrolyte. Magnification plots of selected periods of 2^{nd}–7^{th} cycles and 235^{th}–245^{th} cycles are also shown. Cycling is performed at constant current density of 0.5 mA cm^{-2} with 30 min Li platting/stripping for each cycle. Cycle performance of Li|LFP cells with the GPE and the liquid electrolyte at 1C charge/discharge rate (b) and 2C charge/discharge rate (c). All the tests are performed at ambient temperature (~20 °C).

is important to mention that these processes are typically subtle and impedance range distinction for each individual transfer process is very difficult and complicated. To simplify the analysis, a resistor, R_b, is modeled for bulk ionic resistance of the electrolyte, a parallel resistor, R_{Int}, with non-ideal capacitor, Q, is modeled for the interfacial resistance, and Warburg diffusion, W, is modeled for the semi-infinite diffusion resistance. A similar simplification is also reported in the literature [57,61,62]. The time-constant around 54 Hz (for the GPE) and 36 Hz (for the liquid electrolyte) is related to the diffusion-limited processes related to Li ions within the Li metal and LFP electrode material [59]. The bulk ionic resistance of the electrolyte, R_b, is around 3 Ω and 7 Ω for the liquid electrolyte and the GPE, respectively, and the interfacial resistance, R_{Int}, is approximately 72 Ω and 135 Ω for the Li/GPE/LFP cell and the Li/liquid electrolyte/LFP cell, respectively [59,60]. The interfacial resistance for the electrode/GPE is up to 40% lower than the interfacial resistance for the electrode/liquid electrolyte. The lower resistance value can be due to higher Li ion conductivity of the electrode/GPE interface in comparison to the electrode/liquid electrolyte interface. This could be also correlated to the more inter-connection between the highly elastic, flexible GPE and the Li/LFP electrodes, compared to the mechanically stiff and electrochemically inactive Celgard polypropylene separator.

We have also tracked the impedance evolution after different cycles for the LMBs with the GPE and the liquid electrolyte (Fig. S18). EIS curves show a depressed semicircle at high to medium frequency followed by a slope tail at low frequency. The depressed semicircle is related to the impedance for migration of Li ions through the SEI or passivation layer resistance (R_{SEI}) as well as charge transfer (R_{CT}) at the Li/electrolyte or the electrolyte/LFP interfaces [35]. R_{CT+SEI} increases

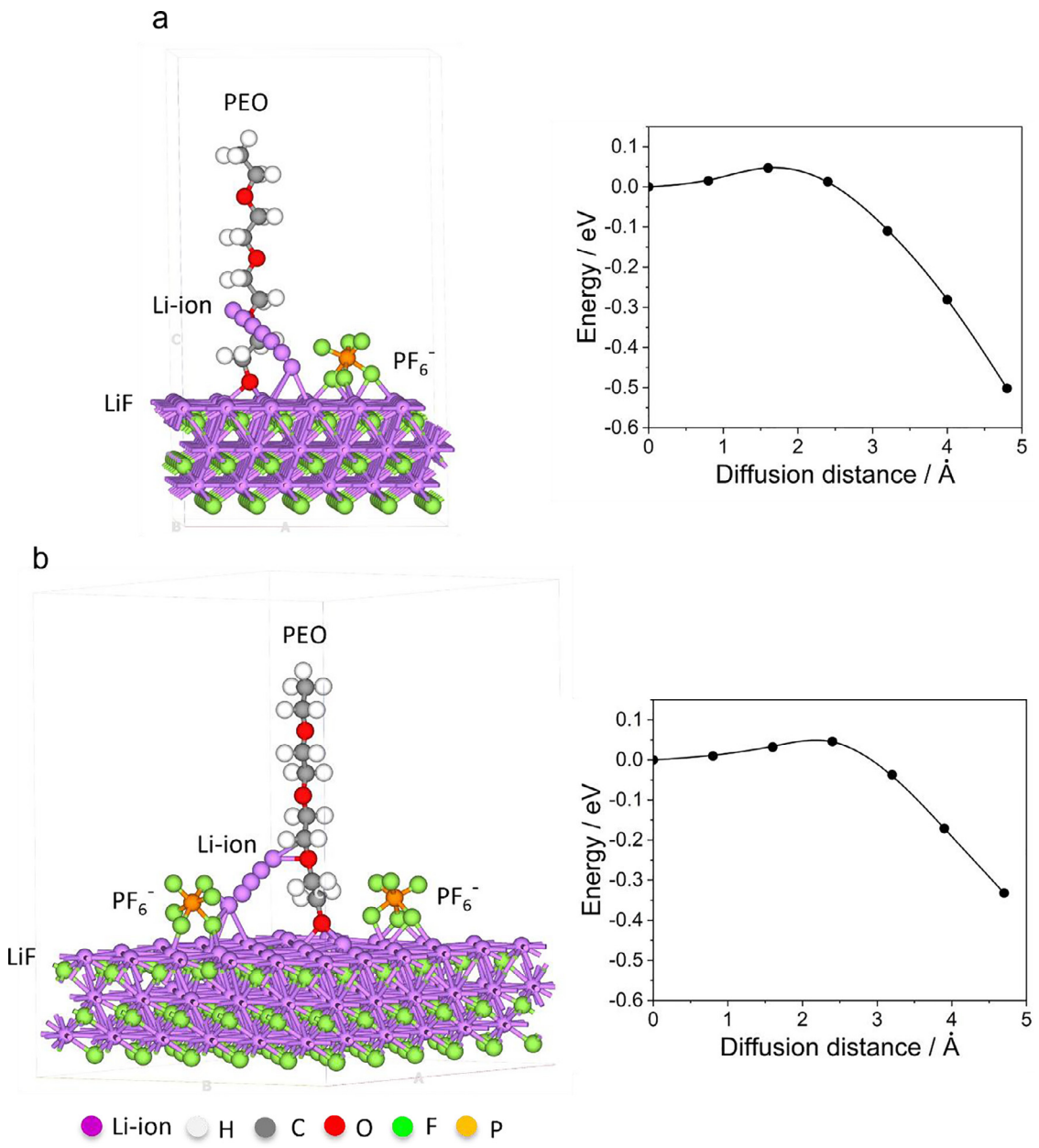

Fig. 9. DFT calculation results. The pathway (left) and the corresponding energetics (right) of Li diffusion onto LiF(111) surface in the presence of one (a) and two (b) hexafluorophosphate (PF_6^-) anions.

for the Li|LFP cell with the liquid electrolyte, which can be due to build-up, reconstruction, and thickening of the SEI layer arising from dendritic Li growth [63]. Due to ultrahigh reducing power of Li metal, parasitic reactions (e.g., Li reacts with carbonate solvents to form Li_2O, C_2H_4 and H_2) inevitably take place at the Li/liquid electrolyte interface to harm the electrochemical performances of LMBs. Thus, the Li/liquid electrolyte interface can be continuously thickened during the battery operation as result of repeated reactions between fresh Li surface and the organic solvents (Fig. 3e). This can lead to an uneven surface morphology of the Li metal anode along with the formation of large electrochemical impedance, which eventually lead to capacity loss and short lifespan of LMBs. In contrast, the R_{CT+SEI} for the Li|LFP cell with the GPE (Fig. S18) show a non-linear change, increase slightly at the earlier cycles followed by a constant decrease [63]. This can be correlated to the stable and conductive SEI layer formed in the GPE. The initial increase of R_{CT+SEI} can be related to the adverse interfacial reactions during initial steps of the SEI formation.

DFT calculations are performed to further understand the molecular-level mechanism behind the uniform Li deposition in the GPE enabled by the LiF-rich interface. Firstly, the most favorable atomic configuration of PEO fragments and the Li salt ($LiPF_6$) on LiF surface are calculated, followed up by the nudge elastic band (NEB) calculations to reveal energy barrier of Li ions diffusion. Following the experimental results shown in Figs. 5 and 6, and consistent with the prior literature reports [64], the DFT calculations are performed over (111) surface orientation of LiF slab as shown in Fig. S19. Several configurations varying PEO and $LiPF_6$ number are considered, and five most stable atomic slabs are selected for further study. As shown in Fig. S19, the atomic slab with one PEO fragment and $LiPF_6$ at the surface of LiF(111) is the most stable configuration. The total energy per atom measure is used to find the most stable atomic structure. Comparing the total energy per atom shown in Fig. S19, the presence of one PF_6^- anion over the LiF(111) surface (Fig. S19b) is beneficial for Li adsorption due to the presence of an excess of a negative charge at the LiF surface. However, with the increase of the

negative charge at the LiF surface (Fig. S19c), the configuration becomes slightly less favorable, similar to the one with more PEO fragments (Fig. S19d). Thus, the second (Fig. S19b) and the third (Fig. S19c) configurations are chosen for further study of the Li ions diffusion. We have studied the favorable pathways for Li deposition at the LiF(111) surface in the presence of one and two PF_6 fragments. Fig. 9 shows the pathway (left) and the energetics (right) of Li adatom diffusion from the PEO bind configuration to LiF(111) surface following our experimental observations (Figs. 5 and 6). It is found that Li deposition onto the LiF(111) surface in the presence of one PF_6 fragment (Fig. 9a) is more favorable than onto the LiF surface with two PF_6 fragments (Fig. 9b) by 0.17 eV. Comparing the activation energy barrier for these two cases (0.045 eV vs. 0.058 eV), we can conclude that these two processes are equally possible, due to very low energy barrier. These findings are consistent with our hypothesis that the excess of negative charge at the LiF(111) surface stimulates Li adsorption, leading to a more uniform electrodeposition.

4. Conclusion

In summary, a novel and efficient GPE is designed for LMBs by the entrapment of liquid electrolytes (1 M $LiPF_6$ in EC/DEC) within the crosslinked m-PEO matrix. In contrast to the liquid electrolyte, a uniform and nondendritic Li electrodeposition in the GPE is observed, as explored by *operando* optical microscopy and SEM. Using cryo-TEM, we have identified the nanoscale structure and chemistry of the SEI layer formed in the liquid electrolyte and the polymeric battery cells. Our findings confirm the mosaic model of SEI, revealing distribution of Li-based inorganic nanocrystals within an amorphous organic/polymeric matrix. In contrast to the thick and mostly amorphous SEI layer with poor Li ion conductivity formed in the liquid electrolyte, the SEI layer formed in the GPE is thin, highly crystalline and rich in LiF, with high Li ion conductivity. Owning to superior electronic insulation and low Li ion diffusion barrier, LiF is considered as an excellent interfacial component. The LiF-rich interface can result in regulation of Li ions transport, leading to a dendrite-free Li platting, confirmed experimentally by optical or electron microscopy and theoretically by DFT calculations. The Li|Li cells with the GPE illustrate a low voltage polarization (~0.1 V) at high current densities (0.5 and 1.0 mA cm^{-2}) and long-term stability of up to 800 cycles at ambient temperature. Furthermore, the Li|LFP cells with the GPE display a specific capacity of ~130 mAh g^{-1} at 2C charge/discharge rate with ~70% capacity retention after 1000 cycles and ~99% CE. Our findings offer new insights for development of stable and highly cycleable gel polymer electrolytes for Li metal batteries.

Declaration of Competing Interest

The authors declare that they have no known competing financial interests or personal relationships that could have appeared to influence the work reported in this paper.

CRediT authorship contribution statement

Vahid Jabbari: Conceptualization, Methodology, Data curation, Writing – original draft, Writing – review & editing, Visualization, Investigation, Validation. **Vitaliy Yurkiv:** Software, Investigation, Data curation, Funding acquisition. **Md Golam Rasul:** Investigation, Data curation. **Mahmoud Tamadoni Saray:** Investigation, Data curation. **Ramin Rojaee:** Investigation, Data curation. **Farzad Mashayek:** Software, Supervision, Funding acquisition. **Reza Shahbazian-Yassar:** Supervision, Project administration, Funding acquisition.

Acknowledgement

R. Shahbazian-Yassar acknowledges the financial support from the National Science Foundation (NSF-CBET award no. 1805938). The present DFT calculations were performed on the High-Performance Computing Cluster Extreme at the University of Illinois at Chicago. The authors also acknowledge the Battery Technology Laboratory of the College of Engineering and Research Resources Center (RRC) at the University of Illinois at Chicago (UIC) especially Director of Electron Microscopy Core, Dr. Fengyuan Shi, the Director of Soft Matter Laboratory at the University of Chicago, Dr. Philip Griffin, and Northwestern University Atomic and Nanoscale Characterization Center (NUANCE) especially NUANCE-TEM facility manager, Dr. Xiaobing Hu, NUANCE-BioCryo facility specialist, Charlene Wilke, and NUANCE-Keckll manager, Dr. Xinqi Chen.

Supplementary materials

Supplementary material associated with this article can be found, in the online version, at doi:10.1016/j.ensm.2022.01.031.

References

[1] J. Liu, Z. Bao, Y. Cui, E.J. Dufek, J.B. Goodenough, P. Khalifah, Q. Li, B.Y. Liaw, P. Liu, A. Manthiram, Y.S. Meng, V.R. Subramanian, M.F. Toney, V.V. Viswanathan, M.S. Whittingham, J. Xiao, W. Xu, J. Yang, X.Q. Yang, J.G. Zhang, Pathways for practical high-energy long-cycling lithium metal batteries, Nat. Energy 4 (2019) 180–186, doi:10.1038/s41560-019-0338-x.

[2] W. Xu, J. Wang, F. Ding, X. Chen, E. Nasybulin, Y. Zhang, J.G. Zhang, Lithium metal anodes for rechargeable batteries, Energy Environ. Sci. 7 (2014) 513–537, doi:10.1039/c3ee40795k.

[3] C.Z. Zhao, X.Q. Zhang, X.B. Cheng, R. Zhang, R. Xu, P.Y. Chen, H.J. Peng, J.Q. Huang, Q. Zhang, An anion-immobilized composite electrolyte for dendrite-free lithium metal anodes, Proc. Natl. Acad. Sci. USA 114 (2017) 11069–11074, doi:10.1073/pnas.1708489114.

[4] C.Z. Zhao, P.Y. Chen, R. Zhang, X. Chen, B.Q. Li, X.Q. Zhang, X.B. Cheng, Q. Zhang, An ion redistributor for dendrite-free lithium metal anodes, Sci. Adv. 4 (2018) 1–9, doi:10.1126/sciadv.aat3446.

[5] P. Bai, J. Guo, M. Wang, A. Kushima, L. Su, J. Li, F.R. Brushett, M.Z. Bazant, Interactions between lithium growths and nanoporous ceramic separators, Joule 2 (2018) 2434–2449, doi:10.1016/j.joule.2018.08.018.

[6] R. Pathak, K. Chen, A. Gurung, K.M. Reza, B. Bahrami, J. Pokharel, A. Baniya, W. He, F. Wu, Y. Zhou, K. Xu, Q. (Quinn) Qiao, Fluorinated hybrid solid-electrolyte-interphase for dendrite-free lithium deposition, Nat. Commun. 11 (2020) 1–10, doi:10.1038/s41467-019-13774-2.

[7] A. Hagopian, M.L. Doublet, J.S. Filhol, Thermodynamic origin of dendrite growth in metal anode batteries, Energy Environ. Sci. 13 (2020) 5186–5197, doi:10.1039/d0ee02665d.

[8] L. Li, M. Wang, J. Wang, F. Ye, S. Wang, Y. Xu, J. Liu, G. Xu, Y. Zhang, Y. Zhang, C. Yan, N.V. Medhekar, M. Liu, Y. Zhang, Asymmetric gel polymer electrolyte with high lithium ion conductivity for dendrite-free lithium metal batteries, J. Mater. Chem. A 8 (2020) 8033–8040, doi:10.1039/d0ta01883j.

[9] A. Pei, G. Zheng, F. Shi, Y. Li, Y. Cui, Nanoscale nucleation and growth of electrodeposited lithium metal, Nano Lett. 17 (2017) 1132–1139, doi:10.1021/acs.nanolett.6b04755.

[10] P. Biswal, S. Stalin, A. Kludze, S. Choudhury, L.A. Archer, Nucleation and early stage growth of Li electrodeposits, Nano Lett. 19 (2019) 8191–8200, doi:10.1021/acs.nanolett.9b03548.

[11] A.A. Assegie, J.H. Cheng, L.M. Kuo, W.N. Su, B.J. Hwang, Polyethylene oxide film coating enhances lithium cycling efficiency of an anode-free lithium-metal battery, Nanoscale 10 (2018) 6125–6138, doi:10.1039/c7nr09058g.

[12] C. Niu, J. Liu, G. Chen, C. Liu, T. Qian, J. Zhang, B. Cao, W. Shang, Y. Chen, J. Han, J. Du, Y. Chen, Anion-regulated solid polymer electrolyte enhances the stable deposition of lithium ion for lithium metal batteries, J. Power Sources 417 (2019) 70–75, doi:10.1016/j.jpowsour.2019.02.004.

[13] W. Fan, N.W. Li, X. Zhang, S. Zhao, R. Cao, Y. Yin, Y. Xing, J. Wang, Y.G. Guo, C. Li, A dual-salt gel polymer electrolyte with 3D cross-linked polymer network for dendrite-free lithium metal batteries, Adv. Sci. 5 (2018), doi:10.1002/advs.201800559.

[14] Y. Zhu, J. Cao, H. Chen, Q. Yu, B. Li, High electrochemical stability of a 3D cross-linked network PEO@nano-SiO2 composite polymer electrolyte for lithium metal batteries, J. Mater. Chem. A 7 (2019) 6832–6839, doi:10.1039/c9ta00560a.

[15] S. Liang, W. Yan, X. Wu, Y. Zhang, Y. Zhu, H. Wang, Y. Wu, Gel polymer electrolytes for lithium ion batteries: Fabrication, characterization and performance, Solid State Ionics 318 (2018) 2–18, doi:10.1016/j.ssi.2017.12.023.

[16] X. Cheng, J. Pan, Y. Zhao, M. Liao, H. Peng, Gel polymer electrolytes for electrochemical energy storage, Adv. Energy Mater. 8 (2018), doi:10.1002/aenm.201702184.

[17] W. Li, Y. Pang, J. Liu, G. Liu, Y. Wang, Y. Xia, A PEO-based gel polymer electrolyte for lithium ion batteries, RSC Adv. 7 (2017) 23494–23501, doi:10.1039/c7ra02603j.

[18] Y. Kang, K. Cheong, K.A. Noh, C. Lee, D.Y. Seung, A study of cross-linked PEO gel polymer electrolytes using bisphenol A ethoxylate diacrylate: Ionic conductivity and mechanical properties, J. Power Sources 119–121 (2003) 432–437, doi:10.1016/S0378-7753(03)00183-6.

[19] M. Liu, Y. Wang, M. Li, G. Li, B. Li, S. Zhang, H. Ming, J. Qiu, J. Chen, P. Zhao, A new composite gel polymer electrolyte based on matrix of PEGDA with high ionic conductivity for lithium-ion batteries, Electrochim. Acta 354 (2020) 136622, doi:10.1016/j.electacta.2020.136622.

[20] M.W. Logan, S. Langevin, B. Tan, A.W. Freeman, C. Hoffman, D.B. Trigg, K. Gerasopoulos, UV-cured eutectic gel polymer electrolytes for safe and robust Li-ion batteries, J. Mater. Chem. A 8 (2020) 8485–8495, doi:10.1039/d0ta01901a.
[21] L. Porcarelli, C. Gerbaldi, F. Bella, J.R. Nair, Super soft all-ethylene oxide polymer electrolyte for safe all-solid lithium batteries, Sci. Rep. 6 (2016) 1–14, doi:10.1038/srep19892.
[22] G. Kresse, J. Furthmüller, Efficient iterative schemes for ab initio total-energy calculations using a plane-wave basis set, Phys. Rev. B - Condens. Matter Mater. Phys. 54 (1996) 11169–11186, doi:10.1103/PhysRevB.54.11169.
[23] J.P. Perdew, J.A. Chevary, S.H. Vosko, K.A. Jackson, M.R. Pederson, D.J. Singh, C. Fiolhais, Erratum: Atoms, molecules, solids, and surfaces: applications of the generalized gradient approximation for exchange and correlation (Physical Review B (1993) 48, 7, (4978)), Phys. Rev. B. 48 (1993) 4978, doi:10.1103/PhysRevB.48.4978.2.
[24] J.P. Perdew, K. Burke, M. Ernzerhof, Generalized gradient approximation made simple, Phys. Rev. Lett. 77 (1996) 3865–3868, doi:10.1103/PhysRevLett.77.3865.
[25] N. Hasan, M. Pulst, M.H. Samiullah, J. Kressler, Comparison of Li+-ion conductivity in linear and crosslinked poly(ethylene oxide), J. Polym. Sci. Part B Polym. Phys. 57 (2019) 21–28, doi:10.1002/polb.24750.
[26] S.P. Ding, K. Xu, S.S. Zhang, T.R. Jow, K. Amine, G.L. Henriksen, Diminution of supercooling of electrolytes by carbon particles, J. Electrochem. Soc. 146 (1999) 3974–3980, doi:10.1149/1.1392579.
[27] N. Wongittharom, T.C. Lee, I.M. Hung, S.W. Lee, Y.C. Wang, J.K. Chang, Ionic liquid electrolytes for high-voltage rechargeable Li/LiNi 0.5Mn1.5O4 cells, J. Mater. Chem. A 2 (2014) 3613–3620, doi:10.1039/c3ta14423b.
[28] H. Yang, G.V. Zhuang, P.N. Ross, Thermal stability of LiPF6 salt and Li-ion battery electrolytes containing LiPF6, J. Power Sources 161 (2006) 573–579, doi:10.1016/j.jpowsour.2006.03.058.
[29] G. Burke, Z. Cao, D.M. Devine, I. Major, Preparation of biodegradable polyethylene glycol dimethacrylate hydrogels via thiol-ene chemistry, Polymers (Basel) 11 (2019), doi:10.3390/polym11081339.
[30] Y. Wang, J. Qiu, J. Peng, J. Li, M. Zhai, One-step radiation synthesis of gel polymer electrolytes with high ionic conductivity for lithium-ion batteries, J. Mater. Chem. A 5 (2017) 12393–12399, doi:10.1039/c7ta02291c.
[31] M.R.N. Nabilah, M.A. Alwi, M.S. Su'ait, M. Imperiyka, S.A. Hanifah, A. Ahmad, N.H. Hassan, M.Y.A. Rahman, Effect of ionic liquid 1-butyl-3-methylimidazolium bis(trifluoromethanesulfonyl)imide on the properties of poly(glycidyl methacrylate) based solid polymer electrolytes, Russ. J. Electrochem. 52 (2016) 362–373, doi:10.1134/S1023193516040091.
[32] J.S. Gnanaraj, E. Zinigrad, L. Asraf, H.E. Gottlieb, M. Sprecher, M. Schmidt, W. Geissler, D. Aurbach, A detailed investigation of the thermal reactions of LiPF[sub 6] solution in organic carbonates using ARC and DSC, J. Electrochem. Soc. 150 (2003) A1533, doi:10.1149/1.1617301.
[33] G. Yang, I.N. Ivanov, R.E. Ruther, R.L. Sacci, V. Subjakova, D.T. Hallinan, J. Nanda, Electrolyte solvation structure at solid-liquid interface probed by nanogap surface-enhanced Raman spectroscopy, ACS Nano (2018), doi:10.1021/acsnano.8b05038.
[34] Q. Wang, C. Yang, Y. Zhang, J. Yang, K. Wu, C. Hu, J. Lu, W. Liu, H. Zhou, Surface-based Li+ complex enables uniform lithium deposition for stable lithium metal anodes, ACS Appl. Energy Mater. 2 (2019) 4602–4608, doi:10.1021/acsaem.9b00929.
[35] Y. Xu, H. Wu, H. Jia, J.G. Zhang, W. Xu, C. Wang, Current density regulated atomic to nanoscale process on Li deposition and solid electrolyte interphase revealed by cryogenic transmission electron microscopy, ACS Nano 14 (2020) 8766–8775, doi:10.1021/acsnano.0c03344.
[36] S. Choudhury, S. Stalin, D. Vu, A. Warren, Y. Deng, P. Biswal, L.A. Archer, Solid-state polymer electrolytes for high-performance lithium metal batteries, Nat. Commun. 10 (2019) 1–8, doi:10.1038/s41467-019-12423-y.
[37] Y. Li, Y. Li, A. Pei, K. Yan, Y. Sun, C.L. Wu, L.M. Joubert, R. Chin, A.L. Koh, Y. Yu, J. Perrino, B. Butz, S. Chu, Y. Cui, Atomic structure of sensitive battery materials and interfaces revealed by cryo–electron microscopy, Science (80-.) 358 (2017) 506–510, doi:10.1126/science.aam6014.
[38] O. Sheng, J. Zheng, Z. Ju, C. Jin, Y. Wang, M. Chen, J. Nai, T. Liu, W. Zhang, Y. Liu, X. Tao, Situ construction of a LiF-enriched interface for stable all-solid-state batteries and its origin revealed by Cryo-TEM, Adv. Mater. 32 (2020) 1–10, doi:10.1002/adma.202000223.
[39] J. Zheng, Z. Ju, B. Zhang, J. Nai, T. Liu, Y. Liu, Q. Xie, W. Zhang, Y. Wang, X. Tao, Lithium ion diffusion mechanism on the inorganic components of the solid-electrolyte interphase, J. Mater. Chem. A 9 (2021) 10251–10259, doi:10.1039/d0ta11444h.
[40] A. Ramasubramanian, V. Yurkiv, T. Foroozan, M. Ragone, R. Shahbazian-Yassar, F. Mashayek, Lithium diffusion mechanism through solid-electrolyte interphase in rechargeable lithium batteries, J. Phys. Chem. C 123 (2019) 10237–10245, doi:10.1021/acs.jpcc.9b00436.
[41] Y. Li, W. Huang, Y. Li, A. Pei, D.T. Boyle, Y. Cui, Correlating structure and function of battery interphases at atomic resolution using cryoelectron microscopy, Joule 2 (2018) 2167–2177, doi:10.1016/j.joule.2018.08.004.
[42] T. Liu, L. Lin, X. Bi, L. Tian, K. Yang, J. Liu, M. Li, Z. Chen, J. Lu, K. Amine, K. Xu, F. Pan, In situ quantification of interphasial chemistry in Li-ion battery, Nat. Nanotechnol. 14 (2019) 50–56, doi:10.1038/s41565-018-0284-y.
[43] X. Cao, X. Ren, L. Zou, M.H. Engelhard, W. Huang, H. Wang, B.E. Matthews, H. Lee, C. Niu, B.W. Arey, Y. Cui, C. Wang, J. Xiao, J. Liu, W. Xu, J.G. Zhang, Monolithic solid–electrolyte interphases formed in fluorinated orthoformate-based electrolytes minimize Li depletion and pulverization, Nat. Energy 4 (2019) 796–805, doi:10.1038/s41560-019-0464-5.
[44] W. Huang, H. Wang, D.T. Boyle, Y. Li, Y. Cui, Resolving nanoscopic and mesoscopic heterogeneity of fluorinated species in battery solid-electrolyte interphases by cryogenic electron microscopy, ACS Energy Lett. 5 (2020) 1128–1135, doi:10.1021/acsenergylett.0c00194.
[45] L. Wang, A. Menakath, F. Han, Y. Wang, P.Y. Zavalij, K.J. Gaskell, O. Borodin, D. Iuga, S.P. Brown, C. Wang, K. Xu, B.W. Eichhorn, Identifying the components of the solid–electrolyte interphase in Li-ion batteries, Nat. Chem. 11 (2019) 789–796, doi:10.1038/s41557-019-0304-z.
[46] J. Janek, W.G. Zeier, A solid future for battery development, Nat. Energy. 1 (2016) 1–4, doi:10.1038/nenergy.2016.141.
[47] A.C. Balazs, T. Emrick, T.P. Russell, Nanoparticle polymer composites: where two small worlds meet, Science (80-.) 314 (2006) 1107–1110, doi:10.1126/science.1130557.
[48] N. Sata, K. Eberman, K. Eberl, J. Maier, Mesoscopic fast ion conduction in nanometre-scale planar heterostructures, Nature 408 (2000) 946–949, doi:10.1038/35050047.
[49] O. Sheng, J. Zheng, Z. Ju, C. Jin, Y. Wang, M. Chen, J. Nai, T. Liu, W. Zhang, Y. Liu, X. Tao, Situ construction of a LiF-enriched interface for stable all-solid-state batteries and its origin revealed by Cryo-TEM, Adv. Mater. (2020) 32, doi:10.1002/adma.202000223.
[50] Q. Zhang, P. Lu, Z. Liu, M.W. Verbrugge, X. Xiao, J. Pan, Y.T. Cheng, B.W. Sheldon, Y. Qi, Synergetic effects of inorganic components in solid electrolyte interphase on high cycle efficiency of lithium ion batteries, Batter. Congr. 2016 (2016) 3–8, doi:10.1149/ma2016-03/2/192.
[51] K.H. Chen, K.N. Wood, E. Kazyak, W.S. Lepage, A.L. Davis, A.J. Sanchez, N.P. Dasgupta, Dead lithium: mass transport effects on voltage, capacity, and failure of lithium metal anodes, J. Mater. Chem. A 5 (2017) 11671–11681, doi:10.1039/c7ta00371d.
[52] K.N. Wood, E. Kazyak, A.F. Chadwick, K.H. Chen, J.G. Zhang, K. Thornton, N.P. Dasgupta, Dendrites and pits: Untangling the complex behavior of lithium metal anodes through operando video microscopy, ACS Cent. Sci. 2 (2016) 790–801, doi:10.1021/acscentsci.6b00260.
[53] S. Xu, K.-H. Chen, N.P. Dasgupta, J.B. Siegel, A.G. Stefanopoulou, Evolution of dead lithium growth in lithium metal batteries: experimentally validated model of the apparent capacity loss, J. Electrochem. Soc. 166 (2019) A3456–A3463, doi:10.1149/2.0991914jes.
[54] R. Carter, E.J. Klein, T.A. Kingston, C.T. Love, Detection of lithium plating during thermally transient charging of Li-ion batteries, Front. Energy Res. 7 (2019) 1–12, doi:10.3389/fenrg.2019.00144.
[55] S. Li, Q. Liu, X. Wang, Q. Wu, L. Fan, W. Zhang, Z. Shen, L. Wang, M. Ling, Y. Lu, Constructing a phosphating-nitriding interface for practically used lithium metal anode, ACS Mater. Lett. 2 (2020) 1–8, doi:10.1021/acsmaterialslett.9b00416.
[56] S.J. Zhang, Z.G. Gao, W.W. Wang, Y.Q. Lu, Y.P. Deng, J.H. You, J.T. Li, Y. Zhou, L. Huang, X.D. Zhou, S.G. Sun, A natural biopolymer film as a robust protective layer to effectively stabilize lithium-metal anodes, Small (2018) 14, doi:10.1002/smll.201801054.
[57] F. Zeng, Y. Sun, B. Hui, Y. Xia, Y. Zou, X. Zhang, D. Yang, Three-dimensional porous alginate fiber membrane reinforced PEO-based solid polymer electrolyte for safe and high-performance lithium ion batteries, ACS Appl. Mater. Interfaces 12 (2020) 43805–43812, doi:10.1021/acsami.0c13039.
[58] H. Dai, X. Gu, J. Dong, C. Wang, C. Lai, S. Sun, Stabilizing lithium metal anode by octaphenyl polyoxyethylene-lithium complexation, Nat. Commun. (2020) 11, doi:10.1038/s41467-020-14505-8.
[59] F.J. Simon, M. Hanauer, F.H. Richter, J. Janek, Interphase formation of PEO20:LiTFSI-Li6PS5Cl composite electrolytes with lithium metal, ACS Appl. Mater. Interfaces 12 (2020) 11713–11723, doi:10.1021/acsami.9b22968.
[60] R. Rojaee, S. Plunkett, M.G. Rasul, M. Cheng, V. Jabbari, R. Shahbazian-Yassar, Interfacial engineering of lithium-polymer batteries with in situ UV cross-linking, InfoMat 3 (2021) 1016–1027, doi:10.1002/inf2.12197.
[61] C. Song, W. Wang, H. Peng, Y. Wang, C. Zhao, H. Zhang, Q. Tang, J. Lv, X. Du, Y. Dou, Improving the electrochemical performance of LiNi0.80Co0.15Al0.05O2 in lithium ion batteries by LiAlO2 surface modification, Appl. Sci. 8 (2018), doi:10.3390/app8030378.
[62] Q. Guo, S. Li, H. Wang, Y. Gao, B. Li, Molten salt synthesis of nano-sized Li4Ti5O12 doped with Fe2O3 for use as anode material in the lithium-ion battery, RSC Adv. 4 (2014) 60327–60333, doi:10.1039/c4ra09813g.
[63] R. Hu, H. Qiu, H. Zhang, P. Wang, X. Du, J. Ma, T. Wu, C. Lu, X. Zhou, G. Cui, A polymer-reinforced SEI layer induced by a cyclic carbonate-based polymer electrolyte boosting 4.45 V LiCoO2/Li metal batteries, Small 16 (2020) 1–8, doi:10.1002/smll.201907163.
[64] S. Panahian Jand, P. Kaghazchi, The role of electrostatic effects in determining the structure of LiF-graphene interfaces, J. Phys. Condens. Matter. (2014) 26, doi:10.1088/0953-8984/26/26/262001.